



HAL
open science

Mechanisms of genetic instability in a single S-phase following whole genome doubling

Simon Gemble, Sara Vanessa Bernhard, Nishit Srivastava, René Wardenaar, Maddalena Nano, Anne-Sophie Macé, Andréa E Tijhuis, Kristina Keuper, Diana C J Spierings, Helfrid Hochegger, et al.

► **To cite this version:**

Simon Gemble, Sara Vanessa Bernhard, Nishit Srivastava, René Wardenaar, Maddalena Nano, et al.. Mechanisms of genetic instability in a single S-phase following whole genome doubling. 2021. hal-03455281

HAL Id: hal-03455281

<https://hal.science/hal-03455281>

Preprint submitted on 29 Nov 2021

HAL is a multi-disciplinary open access archive for the deposit and dissemination of scientific research documents, whether they are published or not. The documents may come from teaching and research institutions in France or abroad, or from public or private research centers.

L'archive ouverte pluridisciplinaire **HAL**, est destinée au dépôt et à la diffusion de documents scientifiques de niveau recherche, publiés ou non, émanant des établissements d'enseignement et de recherche français ou étrangers, des laboratoires publics ou privés.

1 **Mechanisms of genetic instability in a single S-phase following** 2 **whole genome doubling**

3
4
5 Simon Gemble^{1,7}, Sara Vanessa Bernhard², Nishit Srivastava³, René Wardenaar⁴
6 Maddalena Nano¹, Anne-Sophie Macé⁵, Andréa E. Tijhuis⁴, Kristina Keuper², Diana
7 C.J. Spierings⁴, Helfrid Hochegger⁶, Matthieu Piel³, Floris Fojjer⁴, Zuzana Storchová²
8 and Renata Basto^{1,7}.

9
10
11 1- Institut Curie, PSL Research University, CNRS, UMR144, Biology of Centrosomes
12 and Genetic Instability Laboratory, Paris, France.

13
14 2- Department of Molecular Genetics, TU Kaiserslautern, Kaiserslautern, Germany.

15
16 3- Institut Curie and Institut Pierre Gilles de Gennes, PSL Research University,
17 CNRS, UMR 144, Systems Biology of Cell Polarity and Cell Division, Paris, France.

18
19 4- European Research Institute for the Biology of Ageing, University of Groningen,
20 University Medical Center Groningen, Groningen, The Netherlands.

21
22 5- Cell and Tissue Imaging Facility (PICT-IBiSA), Institut Curie, PSL Research
23 University, Centre National de la Recherche Scientifique, Paris, France.

24
25 6- Genome Damage and Stability Centre, School of Life Sciences, University of
26 Sussex, Brighton, UK.

27
28 7- Corresponding authors- simon.gemble@curie.fr and renata.basto@curie.fr
29
30

31 **ABSTRACT**

32
33 Doubling of the full chromosome content -whole genome duplications (WGDs)- is
34 frequently found in human cancers and is responsible for the rapid evolution of
35 genetically unstable karyotypes¹⁻³. It has previously been established that WGDs fuel
36 chromosome instability due to abnormal mitosis owing to the presence of extra
37 centrosomes and extra chromosomes⁴⁻⁸. Tolerance to ploidy changes has been
38 identified in different model organisms and cell types^{5,6,9-12}, revealing long term
39 cellular adaptations that accommodate ploidy increase. Importantly, however, the
40 immediate consequences of WGDs as cells become tetraploid are not known. It also
41 remains unknown whether WGD triggers other events leading to genetic instability
42 (GIN), independently of mitosis. In this study, we induced tetraploidy in diploid
43 genetically stable RPE-1 cells and monitored the first interphase. We found that newly
44 born tetraploids undergo high rates of DNA damage during DNA replication. Using
45 DNA combing and single cell sequencing, we show that replication forks are unstable,
46 perturbing DNA replication dynamics and generating under- and over-replicated
47 regions at the end of S-phase. Mechanistically, we found that these defects result from
48 lack of protein mass scaling up at the G1/S transition, which impairs the fidelity of DNA
49 replication. This work shows that within a single interphase, unscheduled tetraploid
50 cells can accumulate highly abnormal karyotypes. These findings provide an
51 explanation for the GIN landscape that favors tumorigenesis after tetraploidization.

52

53 **MAIN**

54

55 Diploid and stable karyotypes are associated with health and fitness in animals. In
56 contrast, whole genome duplications (WGDs) are linked to genetic instability (GIN) and
57 cancer^{1,2,13}. WGDs promote chromosomal instability (CIN) over time due to abnormal
58 mitosis, contributing to the evolution of aneuploid karyotypes^{3,6,8,14–16}. These represent
59 cancer vulnerabilities with therapeutic potential^{17,18}. Tolerance to ploidy changes has
60 been identified in different model organisms and cell types^{5,6,9–12}, revealing long-term
61 cellular adaptations that accommodate ploidy increase. Importantly, however, the
62 immediate consequences of unscheduled WGDs are not known and their contribution
63 to GIN remains to be identified. This is an essential question because single WGD
64 events such as cytokinesis failure can promote tumorigenesis¹⁹. Identifying the initial
65 defects derived from WGD and the underlying mechanisms establishing GIN in
66 tetraploid cells is thus an important step, which requires understanding failure in
67 maintaining genetic stability. This type of study has the potential to unravel the origins
68 of GIN in one single cell cycle after WGDs.

69

70 **High levels of DNA damage are generated in the first interphase following**
71 **unscheduled Whole Genome Duplication (WGD)**

72 To identify the immediate consequences of WGDs, we induced tetraploidization in the
73 human diploid and genetically stable RPE-1 immortalized cell line, which contains an
74 almost near-diploid chromosome content. Since WGDs can have different origins^{15,20},
75 we developed several approaches to induce tetraploidization through either
76 cytokinesis failure (CF), endoreplication (EnR) or mitotic slippage (MS) (Fig. 1A and
77 methods). While the large majority of cells resulting from CFs contained two nuclei,
78 EnR or MS generated mainly mononucleated tetraploid cells (Fig. 1A-B and Extended
79 data Fig. 1A-I). Importantly, taking together parameters such as cell size, nuclei
80 number and size, and centrosome number, we were able to distinguish diploids from
81 tetraploids in all the strategies used (Fig. 1B and Extended data Fig. 1A-I). For each
82 strategy, a mix of diploid and tetraploid cells was obtained, allowing a comparison of
83 an internal diploid control and the tetraploid population (Fig. 1C-H, and Extended data
84 Fig. 1A-I). Importantly, from all the conditions used to induce WGDs, the large majority
85 of tetraploid cells continued to cycle and enter and exit the first S-phase (see below).
86 Thus, we have generated the conditions required to study the initial and immediate
87 consequences of tetraploidy within the first cell cycle.

88 Using an early marker of DNA double strand breaks - γ H2AX-, we characterized
89 levels of DNA damage in the first interphase following tetraploidization and found high
90 levels in tetraploid cells. Moreover, this was independent of the way tetraploid cells
91 were generated. In contrast, diploid cells treated in the same conditions or untreated
92 diploids showed low levels of DNA damage (Fig. 1C-H, and Extended data Fig. 1A-I,
93 see Extended data Fig. 2A-C for additional methods of generating tetraploidy). While
94 most of the diploid cells exhibited a low number of γ H2AX foci, the percentage of
95 tetraploid cells with more than 10 foci was high (Fig. 1C-H). We found a correlation
96 between the number of γ H2AX foci and the fluorescence intensity levels of this marker
97 (Extended data Fig. 1J). For simplicity, we will include the information of the number
98 of γ H2AX foci per interphase nuclei throughout this study. Since MS generated the
99 highest frequency of tetraploid cells (Extended data Fig. 1A), we chose to present data
100 derived from MS throughout this study. To confirm some of our results, we also used
101 CF or EnR and this will be mentioned in the figure legends and in the methods.

102 Since a tetraploid nucleus contains twice the amount of DNA than a diploid
103 nucleus, we excluded by normalization with nuclear area or nuclear fluorescence
104 intensity, an increase of γ H2AX foci due to increased nuclear size (Extended data Fig.
105 1K-L). Additionally, we confirmed that the high levels of DNA damage found in the first
106 interphase after tetraploidization were not specific to RPE-1 cells, as the diploid BJ
107 fibroblast cell line as well as the pseudo diploid human colon carcinoma HCT116 cell
108 line also displayed high levels of DNA damage upon WGD (Extended data Fig. 2D-E).

109 We next compared the levels of DNA damage detected in tetraploid cells with
110 the levels of DNA damage in diploid cells generated by replication stress (RS). RS is
111 the slowing or stalling of replication forks, which can be induced by high doses of
112 Aphidicolin (APH) or Hydroxyurea (HU), among other challenges ^{21,22}. Interestingly,
113 APH or HU generated comparable levels of DNA damage in diploid cells, when
114 compared to untreated tetraploid cells (Extended data Fig. 1M).

115 Collectively, our results show that a transition from a diploid to tetraploid status
116 after unscheduled WGD, is accompanied by high levels of DNA damage within the first
117 cell cycle.

118

119 **DNA damage and genetic instability in tetraploid cells is generated during S-** 120 **phase in a DNA replication-dependent manner**

121 We then determined the cell cycle stage in which the DNA damage occurs. We
122 followed cell cycle progression right after WGD using the fluorescence ubiquitination
123 cell cycle indicator (FUCCI) system to map the timing of cell cycle progression in
124 tetraploid cells, allowing us to then monitored the number of γ H2AX foci during the first
125 G1 and the first S-phase (Fig. 2A-B and Extended data Fig. 3A). During G1, the number
126 of γ H2AX foci was quite low and comparable to controls. As cells enter S-phase
127 (t=10hrs), a slight increase in the number of foci in tetraploid nuclei could be observed,
128 which increased substantially at the end of S-phase (t=16hrs) (Fig. 2A-B and Extended
129 data Fig. 3A). These results were further confirmed by time lapse imaging using
130 tetraploid RPE-1 cells tagged with H2B-GFP to visualize DNA and 53BP1-RFP, which
131 is a double strand break repair factor ²³ (Extended data Fig. 3B-C and Extended data
132 movies 1-2). To confirm that DNA damage in tetraploid cells was induced during S-
133 phase, we blocked cells at the G1/S transition using high doses of either CDK4/6 or
134 CDK2 inhibitors for 16 hrs (methods). We chose the 16hrs time period because it
135 corresponds to the end of S-phase in the cycling population (Fig. 2A-B). Afterwards,

136 CDKs inhibitors were washed out allowing cell cycle progression (Extended data Fig.
137 3D). G1-arrested tetraploid cells showed low levels of DNA damage, whereas cells
138 released in S-phase exhibited high levels of DNA damage (Extended data Fig. 3D-G).
139 Importantly, a certain proportion of γ H2AX foci of S-phase tetraploid cells partially co-
140 localized with markers of active DNA replication sites visualized by Proliferating Cell
141 Nuclear Antigen (PCNA) and EdU incorporation (Extended data Fig. 3H).

142 To better characterize DNA damage in tetraploid cells during their first
143 interphase, we used other markers of the DNA damage signaling and repair pathways.
144 We found that the number of KU80 and XRCC1 foci, two proteins involved in Non-
145 Homologous End Joining (NHEJ) ²⁴ remained low (Extended data Fig. 4A-B). In
146 contrast, the number of RAD51 foci, a protein involved in homologous recombination
147 (HR), was increased and co-localized with γ H2AX in a fraction of tetraploid cells
148 (Extended data Fig. 4C-D). This was also the case for Replication protein A (RPA) and
149 FANCD2 foci, two markers of RS which also co-localized with γ H2AX foci in tetraploid
150 cells (Extended data Fig. 4E-G). Together, these results demonstrate that tetraploid
151 cells experience high levels of DNA damage during S-phase progression, which are
152 recognized by bonafide DNA damage markers and by the HR repair pathway.

153 Based on these results, we hypothesized that DNA damage in tetraploid cells
154 arises from errors occurring during DNA replication. To test this possibility, we arrested
155 cells in G1 as described above (Extended data Fig. 3D). We then released them in the
156 presence of very low doses of APH or PHA, a Cdc7 inhibitor. We used low doses of
157 these compounds to inhibit DNA replication (detected by absence of EdU) without
158 generating DNA damage (methods). These conditions resulted in the inhibition of DNA
159 replication, albeit maintaining the biochemical activity typical of the S-phase nucleus.
160 Strikingly, the levels of DNA damage in tetraploid cells were dramatically decreased
161 when DNA replication was inhibited (Fig. 2C-D and Extended data Fig. 4H-J).
162 Importantly, in the few tetraploid cells that escaped DNA replication inhibition -
163 revealed by high EdU incorporation - a high number of γ H2AX foci were noticed
164 (Extended data Fig. 4K-L), confirming the correlation between DNA replication and
165 DNA damage in tetraploid cells.

166 To characterize DNA replication, we established RPE-1 cell lines stably
167 expressing PCNA chromobodies. We showed that expression of PCNA chromobodies
168 does not affect cell cycle progression in RPE-1 cells, confirming its suitability to follow
169 DNA replication by live imaging (Extended data Fig. 4M). Using this cell line, we

170 performed quantitative 4D live imaging of endogenous DNA replication in diploid and
171 tetraploid cells (methods). Surprisingly, the comparison between the total number of
172 PCNA foci during S-phase in diploid and tetraploid RPE-1 cells, revealed a lack of
173 scaling up with DNA content (Fig. 2E-G), also observed by quantifying the number of
174 EdU foci (Extended data Fig. 4N). This result suggests that fewer replication sites were
175 activated in tetraploid S-phase cells, when compared with diploid cells. The volume of
176 PCNA foci was also lower in tetraploid cells (Fig. 2H). Moreover, timelapse analysis of
177 PCNA dynamics revealed additional differences. As diploid cells enter S-phase, an
178 exponential increase in the number of active replication sites was noticed, which was
179 maintained before undergoing a steep, almost abrupt decreased (Fig. 2E-I, Extended
180 data Fig. 5A and Extended data movie 3). In contrast, in tetraploid cells the increase
181 in the number of active sites was more gradual, and the signals associated with DNA
182 lingered for extended periods of time. Furthermore, the dissociation of PCNA from the
183 DNA in tetraploid cells occurred much later and also in a progressive manner (Fig. 2E-
184 I, Extended data Fig. 5A and Extended data movie 4). In line with this, by analyzing
185 PCNA patterns as a readout of early and late S-phase²⁵, we showed that tetraploid
186 cells spent more time in early S-phase compared to late S-phase (Extended data Fig.
187 4O). Surprisingly, even if S-phase was longer in tetraploid cells when compared to
188 diploid cells (Extended data Fig. 4P), this was not sufficient to scale the number of
189 active replication sites with DNA content. These results suggest that DNA replication
190 in tetraploid cells is impaired due to both a lack of scaling up in the number of active
191 replication sites and to a delayed DNA replication timing.

192 To ascertain if these defects impacted replication fork progression, we
193 performed DNA combing, which allows the visualization of replication origins in single
194 DNA fibers²⁶. We failed to obtain fibers of the required quality in RPE-1 cells despite
195 several attempts. To overcome this problem, we performed DNA combing in HCT116
196 cells since they also showed high levels of DNA damage within the first interphase
197 (Extended data Fig. 2E). Inter-origin distances were not affected in tetraploid cells,
198 however, and surprisingly, median fork speed was increased in tetraploid cells (Fig. 2J
199 and Extended data Fig. 4Q). Further, a high increase in the percentage of unstable
200 forks was also detected (Fig. 2J). These results show that the replication dynamics is
201 perturbed in tetraploid cells when compared to diploid cells.

202 Since S-phase progression errors and inaccurate DNA replication are linked
203 with a pleiotropy of DNA structural abnormalities, we assessed if unscheduled

204 tetraploidy was associated with abnormal karyotypes. We FACS sorted tetraploid from
205 diploid cells (see below, Fig. 3C) in G1 and at the G2/M transition to perform single cell
206 DNA sequencing (ssDNAseq) (methods). Normalization of the under and over
207 replicating regions in G1 and G2/M diploid cells revealed already whole chromosome
208 deviations in a certain number of cells. When present, they span along almost all
209 chromosomes of a given cell (Extended data Fig. 5B). In G1 tetraploid cells, over
210 replicated regions (5n) could also be identified, but these were restricted to a few
211 chromosomes and might be explained by a caveat of the method (cells have initiated
212 S-phase but were still selected as G1 by the FACS profile). Striking, however in G2/M
213 tetraploid cells over duplicating chromosomes (> 10) could be identified in addition to
214 frequent over and under replicated regions (9n, 7n and 4n) (Fig. 2K). In agreement
215 with this variability and the extent of copy number deviations, both aneuploidy score
216 and heterogeneity score were increased in G2/M tetraploid cells when compared to
217 G2/M diploid cells (Aneuploidy score: 0.275 vs 0.102; Heterogeneity score 0.319 vs
218 0.158 respectively) (methods).

219 Together, our results show that unscheduled tetraploid cells cannot sustain
220 normal DNA replication as they fail to scale proportionally the number of active
221 replication sites and replication timing. Defects in S-phase result in the generation of
222 highly aberrant karyotypes, demonstrating a causal relationship between
223 tetraploidization and GIN within a single S-phase.

224

225 **Lack of G1 lengthening in tetraploid cells leads to unprepared S-phase**

226 The massive GIN described above, together with abnormal DNA replication dynamics,
227 suggested that newly born tetraploid cells undergo the first S-phase in a non-optimal
228 manner. We reasoned that cells might enter S-phase without the required protein
229 levels to replicate a tetraploid genome. In principle, doubling the whole set of
230 chromosomes should lead to an overall doubling of transcripts and protein translation,
231 so that tetraploid cells should scale up by a factor of 2. To determine if cell mass was
232 increased in tetraploid cells at the G1-S transition, we combined quantitative phase
233 imaging with the cell cycle sensor Fucci, which allows recording of mass measure
234 trajectories through the cell cycle at the single cell level²⁷. We found that the proportion
235 of mass added during G1 was lower in tetraploid cells compared to diploid cells (Fig.
236 3A-B). These results establish that newly born tetraploid cells are not able to scale
237 together protein and DNA content during the first G1 upon WGD. We next tested the

238 total levels of key S-phase components. To do so, we used a recently developed
239 protocol that enables to sort and isolate tetraploid from diploid cells based on FUCCI
240 and DNA content from a common population (Fig. 3C and Extended data Fig. 6A,
241 methods). Protein extracts from the two cell populations at the G1/S transition were
242 then probed by western blot. The same number of cells was loaded for diploid and
243 tetraploid conditions. Normalization of the chromatin associated H2B variant and the
244 cytoskeleton component Actin showed an increase in these two protein levels
245 consistent with DNA doubling (Fig. 3D-E and Extended data Fig. 6B). In stark contrast,
246 essential S-phase DNA replication factors such as the origin recognition complex 1
247 (ORC1) involved in the recognition of replication origins ²⁸, the minichromosome
248 maintenance 2 (MCM2) helicase ²⁹, CDC45, a member of the active helicase complex
249 ³⁰, and PCNA did not scale up in tetraploid cells (Fig. 3D-F). Combined with quantitative
250 phase imaging data, these results suggest that tetraploid cells do not contain the
251 required protein levels to sustain timely and successful DNA replication during S-
252 phase.

253 In normal proliferative cell cycles, the growth phase occurring during G1 phase
254 prepares cells for DNA replication allowing the expression and accumulation of key S-
255 phase regulators ^{31,32}. We reasoned that a short G1 duration could account for
256 transition to S-phase in an unprepared manner, which is supported by the fact that
257 tetraploid cells did not scale up protein content with DNA doubling (Fig. 3A-F). Indeed,
258 time lapse analysis of tetraploid cells just after birth indicated only a slight increase in
259 G1 duration, which did not scale with DNA content when compared to diploid cells (Fig.
260 3G). Further, while we observed a significant correlation between cell mass and G1
261 duration in diploid cells, also described in other diploid conditions ³³, this correlation
262 was absent in tetraploid cells suggesting that G1 duration is not dependent of cell mass
263 in tetraploid cells (Fig. 3H).

264 We next tested if imposing G1 lengthening was translated by increased protein
265 levels of S-phase factors and thus in principle enabled error-free DNA replication in
266 tetraploid cells. To test this model, we delayed S-phase entry using very low doses of
267 CDK4/6 or CDK2 inhibitors. These conditions were different from the ones described
268 above used to synchronize cells in G1. Indeed, while high doses of these inhibitors
269 result in a biochemical arrest, low inhibitor doses result in G1 lengthening ^{34,35}. The
270 different impact of high and low doses of CDK4/6 or CDK2 inhibitors could be noticed
271 by differences in the expression levels of DNA replication factors. Indeed, after G1

272 lengthening the levels of DNA replication factors scaled up with DNA content in
273 tetraploid cells, which was not the case when cells were arrested in G1 (Fig. 3I-K vs
274 3D-F). Consistent with these findings, after G1 lengthening the number and volume of
275 active replication sites in the subsequent S-phase visualized by monitoring PCNA or
276 EdU foci scaled up with DNA content in tetraploid cells (Extended data Fig. 6C-E).
277 Moreover, after G1 extension, PCNA dynamic behavior in tetraploid cells was
278 comparable to diploid cells (Fig. 3L and Extended data Fig. 6F and I and Extended
279 data movies 5-6). Even if the time spent in S-phase was not altered after G1
280 lengthening, we observed that increasing G1 duration restored the ratio between early
281 and late S-phase in tetraploid cells, suggesting that DNA replication timing was
282 reinstated (Extended data Fig. 6G-H). Strikingly, G1 lengthening was sufficient to
283 significantly reduce DNA damage in tetraploid S-phase cells (Fig. 3M and Extended
284 data Fig. 6J-L).

285 Altogether, our data show that tetraploid cells transition from G1 to S-phase
286 prematurely without undergoing scaling of global protein mass, and so they enter in S-
287 phase with insufficient amounts of DNA replication factors. This impacts the dynamics
288 and fidelity of DNA replication, generating DNA damage. Importantly, extension of G1
289 is sufficient to increase the levels of key DNA replication factors, which results in a
290 significant decrease in DNA damage in tetraploid cells.

291
292 **G1 lengthening or increased E2F1 levels are sufficient to rescue GIN in tetraploid**
293 **cells and in polyploid cells *in vivo***

294 From yeast to mammals, the transition from G1 to S-phase is negatively regulated by
295 members of the retinoblastoma (Rb) protein family, which sequesters the transcription
296 factor E2F1^{31,32,36-38}. E2F1 targets several genes required for entry into S-phase and
297 DNA replication factors. Since a short G1 does not prepare tetraploid cells for S-phase,
298 we reasoned that increased levels of E2F1 might override the G1 lengthening defect.
299 We thus expressed E2F1 in diploid cells (Extended data Fig. 7A), allowing to increase
300 the expression of DNA replication proteins just before generating tetraploid cells.
301 Importantly, this was sufficient to rescue the levels of DNA damage in tetraploid cells
302 (Fig. 4A-B).

303 We recently characterized an *in vivo* model to study the consequences of
304 polyploidy in *Drosophila* neural stem cells also called neuroblasts (NBs) in the
305 developing brain³⁹. These cells are normally diploid, but through repeated CF can

306 generate highly polyploid NBs (here referred to as unscheduled polyploidy) much
307 beyond the tetraploidization status (Fig. 4C-D and Extended data Fig. 7B). A key
308 prediction of our findings is that polyploid NBs should also accumulate high levels of
309 DNA damage *in vivo*. To test this prediction, we determined the levels of DNA damage
310 in unscheduled polyploid NBs during interphase using antibodies against γ H2Av to
311 determine the γ H2Av index (methods). We compared it with diploid NBs and the
312 programmed polyploid cells from the *Drosophila* salivary gland, which are extremely
313 large and accumulate more than 2000 chromosomes⁴⁰. This represents a 250- fold
314 increase in DNA content, when compared with diploid *Drosophila* cells, which contain
315 only 8 chromosomes. Interestingly, interphase polyploid NBs displayed high levels of
316 DNA damage, which was not the case in diploid NBs or polyploid cells from the salivary
317 gland (Fig. 4D-E and Extended data Fig. 7C). We next increased the levels of E2F1
318 and Rb by over-expressing (OE) in a tissue-specific manner using the UAS-Gal4
319 system. E2F1OE increases the expression of cell cycle regulators, while RbOE
320 increases G1 lengthening^{41,42}. Strikingly, this was sufficient to decrease substantially
321 the levels of DNA damage in unscheduled polyploid NBs *in vivo* (Fig. 4F-G and
322 Extended data Fig. 7D).

323 Taken together, these data show that *in vivo* unscheduled polyploidy is a source
324 of DNA damage and GIN, which can be inhibited by increased E2F1 or Rb levels.
325 These results put forward the idea that lack of cell cycle readjustment promotes GIN
326 and the accumulation of highly complex karyotypes in cells that are not programmed
327 to increase their DNA content (Fig. 4H).

328
329 Here, we analyzed the initial defects following WGD and identified a very early
330 window of high GIN that could promote acquisitions of multiple mutations making it
331 possible to bypass cell cycle controls while promoting tetraploid cell survival. Our
332 results are consistent with a model where tetraploid cells transit through the first cell
333 cycle without preparing the duplication of increased DNA content (Fig. 4H). We found
334 defective fork progression rates in tetraploid cells, which surprisingly seem to progress
335 faster than in diploid cells. Although the increased rates remain to be explained, these
336 may contribute to RS and GIN as recently shown upon PARP inhibition⁴³ or in
337 response to decreased levels of MCM proteins⁴⁴. Strikingly, G1 extension or the
338 increase in the expression levels of cell cycle proteins *in vivo* lowered considerably the
339 high DNA damage levels of extreme polyploid cells such as the ones generated by

340 repeated CF. These results highlight the importance of keeping constant scaling up
341 between DNA and protein content to ensure genetic stability and cell homeostasis.

342 The most surprising finding of this study is the lack of scaling up between DNA
343 and protein content immediately after tetraploidization. In physiological conditions,
344 such as during animal development, WGDs and polyploidization lead to an overall
345 scaling up of cell mass and DNA content to favor increase in secretion and metabolic
346 activity for example ^{20,45,46}. Our work shows that unscheduled tetraploid or polyploid
347 cells do not increase cell mass as expected. Why certain key cell cycle and DNA
348 replication factors fail to be expressed at levels that allow optimal DNA replication
349 remains to be explained. Importantly, however these results show that an immediate
350 consequence of unscheduled genome doubling is loss of genetic integrity within a
351 single S-phase. Interestingly, studies performed on stable tetraploid cells have shown
352 a remarkable scaling up between protein and DNA content after long term adaptation
353 ^{47,48}. It is tempting to propose that in non-physiological conditions, as the ones studied
354 here, newly born tetraploids do not “feel” the increase in DNA content and so, cannot
355 adapt G1 duration or protein content in order to replicate a 4N genome. It will be
356 interesting to identify the molecular mechanisms that promote ploidy increase while
357 maintaining genetic stability and cell homeostasis.

358

359 **Acknowledgments**

360 The authors acknowledge the Cell and Tissue Imaging platform (PICT-IBiSA), member
361 of the French National Research Infrastructure France-BioImaging (ANR10-INBS-04)
362 and the Nikon Imaging center from Institut Curie for microscopy. We thank L.
363 Guyonnet, A. Chipont and C. Guerrin from the Cytometry platform of Institut Curie. We
364 thank V. Marthiens, S. Lambert, E. Schwob, J.S. Hoffmann, D. Fachinetti, M. Budzyk,
365 F. Edwards, O. Goundiam, G. Fantozzi, R. Salamé, A. Goupil and C. Chen for helpful
366 discussions and/or comments on the manuscript. This work was supported by
367 FOR2800/STO918-7 to Z.S, ERC CoG (ChromoNumber-LS3, ERC-2016-COG) for
368 R.B, Institut Curie and the CNRS. The Basto lab is a member of the Cell(n)Scale
369 Labex.

370

371 **Author contributions**

372 S.G. and R.B. conceived the project and wrote the manuscript. S.G. did most of the
373 experiments and data analysis presented here. M.N. did the initial observations of high
374 levels of DNA damage in *Drosophila* polyploid NBs. S.V.B., K.K. and Z.S. did the DNA
375 combing. R.W., A.E.T., D.C.J.S. and F.F. did the scSeq and BI analysis. A.S.M helped
376 with image quantifications and analysis. N.S. and M.P. performed the quantitative
377 phase imaging experiments and analysis and H.H. contributed with unpublished cell
378 lines. All authors read and comment on the manuscript.

379

380 **METHOD DETAILS:**

381 **Cell culture, generation of cell lines and treatments:**

382 *Cell culture:*

383 Cells were maintained at 37°C in a 5% CO₂ atmosphere. hTERT RPE-1 cells (ATCC
384 Cat# CRL-4000, RRID:CVCL_4388) and HEK293 cells (ATCC Cat# CRL-1573,
385 RRID:CVCL_0045) were grown in Dulbecco's modified medium (DMEM) F12 (11320-
386 033 from Gibco) containing 10% fetal bovine serum (GE Healthcare), 100 U/ml
387 penicillin, 100 U/ml streptomycin (15140-122 from Gibco). BJ cells (ATCC Cat# CRL-
388 4001, RRID:CVCL_6573) and HCT116 cells (ATCC Cat# CCL-247,
389 RRID:CVCL_0291) were grown in Dulbecco's modified medium + GlutaMAX (61965-
390 026 from Gibco) containing 10% fetal bovine serum (GE Healthcare), 100 U/ml
391 penicillin, 100 U/ml streptomycin (15140-122 from Gibco).

392

393 All cells were routinely checked for mycoplasma infection.

394

395 *Generation of RPE-1 PCNA^{chromo} stable cell line:*

396 RPE-1 cells were transfected with 10µg Cell Cycle-Chromobody® plasmid (TagRFP)
397 (From Chromotek, Planegg, Germany) using JET PRIME kit (Polyplus Transfection,
398 114-07) according to the manufacturer protocol. After 24 hours, 500µg/ml G418
399 (4727878001 from Sigma Aldrich) was added to the cell culture medium and then
400 clones expressing PCNA chromobodies were selected.

401

402 *Generation of a RPE-1 Fucci or RPE-1 CCNB1^{AID} Fucci stable cell line:*

403 To produce lentiviral particles, HEK293 cells were transfected with 4µg pBOB-EF1-
404 FastFucci-Puro (86849 from Addgene, RRID:Addgene_86849) + 4µg pMD2.G
405 (12259 from Addgene, RRID:Addgene_12259) + 4µg psPAX2 (12260 from Addgene,
406 RRID:Addgene_12260) using FuGENE HD Transfection Reagent (E2311 from
407 Promega) in OptiMEM medium (51985034 from ThermoFisher). Cells were incubated
408 at 37°C in a 5% CO₂ atmosphere for 16 hours and then growth media were removed
409 and replaced by 5 ml fresh OptiMEM. The following day, viral particles were isolated
410 by filtering the medium containing the viral particles through a 0.45µm filter (16537
411 from Sartorius stedim biotech). Then, RPE-1 or RPE-1 CCNB1^{AID} 49 cells were
412 incubated with viral particles in the presence of 8µg/ml polybrene (sc-134220 from
413 Santa Cruz) at 37°C in a 5% CO₂ atmosphere for 24 hours. RPE-1 GFP and RFP-

414 positive cells were then collected using Sony SH800 FACS (BD FACSDiva Software
415 Version 8.0.1). RPE-1 or RPE-1 CCNB1^{AID} clones expressing FUCCI were selected
416 and the cell lines were established from one single clone.

417 pBOB-EF1-FastFUCCI-Puro was a gift from Kevin Brindle & Duncan Jodrell (Addgene
418 plasmid # 86849 ; <http://n2t.net/addgene:86849> ; RRID:Addgene_86849)⁵⁰.

419

420 *Generation of RPE-1 GFP-53BP1 RFP-H2B stable cell line:*

421 This cell line was obtained as described below. Briefly, to produce lentiviral particles,
422 HEK293 cells were transfected with 4µg pSMPUW-IRIS-Neo-H2BmRFP (Fachinetti
423 Lab) + 4µg pMD2.G (12259 from Addgene, RRID:Addgene_12259) + 4µg psPAX2
424 (12260 from Addgene, RRID:Addgene_12260). Then, RPE-1 cells were incubated with
425 viral particles and RPE-1 RFP-positive cells were collected using Sony SH800 FACS
426 (BD FACSDiva Software Version 8.0.1). RPE-1 clones expressing RFP-H2B were
427 selected, and the cell line was established from one single clone.

428 Then, new lentiviral particles were produced by transfecting HEK293 cells with 4µg
429 Apple-53BP1trunc (69531 from Addgene, RRID:Addgene_69531) + 4µg pMD2.G
430 (12259 from Addgene, RRID:Addgene_12259) + 4µg psPAX2 (12260 from Addgene,
431 RRID:Addgene_12260). RPE-1 RFP-H2B cells were incubated with viral particles and
432 RPE-1 clones expressing both RFP-H2B and GFP-53BP1 were selected using flow
433 cytometry (FACS SH800 from Sony) and the cell line was established from one single
434 clone.

435 Apple-53BP1trunc was a gift from Ralph Weissleder (Addgene plasmid # 69531 ;
436 <http://n2t.net/addgene:69531> ; RRID:Addgene_69531)⁵¹.

437

438 *Generation of tetraploid cells:*

439 **Mitotic slippage using drugs:** cells were incubated with DMSO (D8418 from Sigma
440 Aldrich) or with 50µM monastrol (S8439 from Selleckchem) + 1µM MPI-0479605
441 (S7488 from Selleckchem) for at least two hours. This approach was used in Fig. 1B-
442 D; Fig. 2A-I; Fig. 3L-M; Fig. 4A-B; Extended data Fig. 1A-C and I-M; Extended data
443 Fig. 2D-E; Extended data Fig.3B-E and G-H; Extended data Fig. 4A-H; K and N-P;
444 Extended data Fig. 5A; Extended data Fig. 6C-H and J-L; Extended data Fig. 7A.

445 **Mitotic slippage using genetic tools:** CCNB1 depletion in RPE CCNB1^{AID} cells was
446 induced as described before⁴⁹. Briefly, cells were treated with 2µg/ml doxycycline
447 (D3447 from Sigma Aldrich) + 3µM asunaprevir (S4935 from Selleckchem) for 2 hours.

448 Then, 500 μ M auxin (I5148 from Sigma Aldrich) was added to the cell culture medium
449 for at least 4 hours. This approach was used in Fig1K; Fig. 3A-K; Extended data Fig.
450 2A; Extended data Fig. 6A-B.

451 **Cytokinesis failure using drugs:** cells were incubated with 10 μ M genistein (G6649
452 from Sigma Aldrich) for at least two hours. This approach was used in Fig. 1E-F;
453 Extended data Fig. 1DF; Extended data Fig. 2D-E; Extended data Fig. 3A and F;
454 Extended data Fig. 3I-J; Extended data Fig. 6I. Alternatively, cell were incubated with
455 0.75 μ M Dihydrocytochalasin D (D1641 from Sigma-Aldrich) for 1 hour. This approach
456 was used in Fig. 2J; Extended data Fig. 2B; Extended data Fig. 4Q.

457 **Endoreplication using drugs:** cells were incubated with 10 μ M SP600125 (S1460
458 from Selleckchem) for at least two hours. This approach was used in Fig. 1G-H and
459 Extended data Fig. 1G-I.

460 **Endoreplication using genetic tools:** CCNA2 depletion in RPE CCNA2^{AID} cells was
461 induced as described before⁴⁹. Briefly, cells were treated with 2 μ g/ml doxycycline
462 (D3447 from Sigma Aldrich) for 2 hours. Then, 500 μ M auxin (I5148 from Sigma
463 Aldrich) + 3 μ M asunaprevir (S4935 from Selleckchem) was added to the cell culture
464 medium for at least 4 hours. This approach was used in Extended data Fig. 2C.

465

466 *Cell cycle synchronization and DNA replication inhibition:*

467 Cells were treated with 1 μ M palbociclib (Cdk4/6 inhibitor, S1579 from Selleckchem),
468 with 0.5 μ M abemaciclib (Cdk4/6 inhibitor, S5716 from Selleckchem) or with 1 μ M
469 K03861(Cdk2 inhibitor, S8100 from Selleckchem) for 16 hours to synchronize cells at
470 G1/S transition and were collected (indicated by “G1 arrest” in the figures).
471 Alternatively, cells were then washed five times using PBS 1X and released in S-phase
472 for 10 hours before being collected (indicated by “Release in S-phase” in the figures).
473 To inhibit DNA replication, cells were released in S-phase in the presence of low doses
474 of Aphidicolin (APH, A0781 from Sigma-Aldrich), a DNA replication polymerase
475 inhibitor, or of PHA767491 (PZ0178 from Sigma-Aldrich), a Cdc7 inhibitor (indicated
476 by “Release in S-phase + APH” or “Release in S-phase + PHA”, respectively, in the
477 figures). Doses were chosen to significantly decrease EdU incorporation without
478 affecting the levels of DNA damage.

479

480 *Treatments:*

Names:	Companies:	Targets:	References:	Concentrations:
Auxin	Sigma	AID system	I5148	500 μ M
Doxycycline	Sigma Aldrich	AID system	D3447	2 μ g/ml
Asunaprevir	Selleckchem	AID system	S4935	3 μ M
Monastrol	Selleckchem	Eg5	S8439	50 μ M
MPI-0479605	Selleckchem	MPS1	S7488	1 μ M
Genistein	Sigma Aldrich	MKLP1	G6649	10 μ M
SP600125	Selleckchem	JNK	S1460	10 μ M
Abemaciclib	Selleckchem	CDK4/6	S5716	50nM or 0.5 μ M
K03861	Selleckchem	CDK2	S8100	400nM or 1 μ M
Palbociclib	Selleckchem	CDK4/6	S1579	120nM or 1 μ M
Aphidicolin	Sigma Aldrich	DNA polymerase	A0781	0.4 μ M or 1 μ M
Hydroxyurea	Selleckchem	RNR	S1896	2mM
PHA 767491	Sigma Aldrich	Cdc7	PZ0178	1 μ M
RO3306	Calbiochem	CDK1	217699	10 μ M
Dihydrocytochalasin D	Sigma Aldrich	Actin	D1641	0.75 μ M
5'-Chloro-2'-deoxyuridine (CldU)	Sigma Aldrich	DNA	C6891	100 μ M
5'-Iodo-2'-deoxyuridine (IdU)	Sigma Aldrich	DNA	I7125	100 μ M

481

482 **Fly husbandry and fly stocks:**

483 Flies were raised on cornmeal medium (0.75% agar, 3.5% organic wheat flour, 5.0%
484 yeast, 5.5% sugar, 2.5% nipagin, 1.0% penicillin-streptomycin and 0.4% propionic
485 acid). Fly stocks were maintained at 18°C. Crosses were carried out in plastic vials
486 and maintained at 25°C. Stocks were maintained using balancer inverted
487 chromosomes to prevent recombination. Stocks used in this study: *sqh1*⁵², *pavarotti*
488 RNAi (BL#42573 from Bloomington Drosophila Stock Center, Indiana University, IN,
489 USA)³⁹, UAS-E2F1 (F001065 from FlyORF, Zurich, Switzerland) and UAS-Rb (BL#
490 50746 from Bloomington Drosophila Stock Center, Indiana University, IN, USA).

491 In all experiments, larvae were staged to obtain comparable stages of development.
492 Egg collection was performed at 25°C for 24 hours. After development at 25°C, third
493 instar larvae were used for dissection.

494

495 **Immunofluorescence microscopy and antibodies:**

496 *Preparation and imaging of human cells*

497 Cells were plated on cover slips in 12-well plates and treated with the indicated drugs.
498 To label cells, they were fixed using 4% of paraformaldehyde (15710 from Electron
499 Microscopy Sciences) + Triton X-100 (2000-C from Euromedex) 0,1% in PBS (20 min
500 at 4°C). Then, cells were washed three times using PBS-T (PBS 1X + 0,1% Triton X-
501 100 + 0,02% Sodium Azide) and incubated with PBS-T + BSA (04-100-812-C from
502 Euromedex) 1% for 30 min at RT. After three washes with PBS-T + BSA, primary and
503 secondary antibodies were incubated in PBS-T + BSA 1% for 1 hr and 30 min at RT,
504 respectively. After two washes with PBS, cells were incubated with 3 µg/ml DAPI (4',6-
505 diamidino-2-phenylindole; D8417 from Sigma Aldrich) for 15 min at RT. After two
506 washes with PBS slides were mounted using 1.25% n-propyl gallate (Sigma, P3130),
507 75% glycerol (bidistilled, 99.5%, VWR, 24388-295), 23.75% H₂O.

508

509 Images were acquired on an upright widefield microscope (DM6B, Leica Systems,
510 Germany) equipped with a motorized XY and a 40X objective (HCX PL APO 40X/1,40-
511 0,70 Oil from Leica). Acquisitions were performed using Metamorph software
512 (Molecular Devices, USA) and a sCMOS camera (Flash 4V2, Hamamatsu, Japan).
513 Stacks of conventional fluorescence images were collected automatically at a Z-
514 distance of 0.5 µm (Metamorph software; Molecular Devices, RRID:SCR_002368).
515 Images are presented as maximum intensity projections generated with ImageJ
516 software (RRID:SCR_002285).

517

518 *Whole mount tissue preparation and imaging of Drosophila larval brains*

519 Brains or Salivary glands from third instar larvae were dissected in PBS and fixed for
520 30 minutes in 4% paraformaldehyde in PBS. They were washed three times in PBST
521 0.3% (PBS, 0.3% Triton X-100 (T9284, Sigma), 10 minutes for each wash) and
522 incubated for several hours in agitation at room temperature (RT) and O/N at 4°C with
523 primary antibodies at the appropriate dilution in PBST 0.3%. Tissues were washed
524 three times in PBST 0.3% (10 minutes for each wash) and incubated O/N at 4°C with
525 secondary antibodies diluted in PBST 0.3%. Brains and salivary glands were then
526 washed two times in PBST 0.3% (30 minutes for each wash), rinsed in PBS and
527 incubated with 3 µg/ml DAPI (4',6-diamidino-2-phenylindole; D8417 from Sigma

528 Aldrich) at RT for 30min. Brains and salivary glands were then washed in PBST 0.3%
529 at RT for 30 minutes and mounted in mounting media. A standard mounting medium
530 was prepared with 1.25% n-propyl gallate (Sigma, P3130), 75% glycerol (bidistilled,
531 99.5%, VWR, 24388-295), 23.75% H₂O.

532

533 Images were acquired on a spinning disk microscope (Gataca Systems, France).
534 Based on a CSU-W1 (Yokogawa, Japan), the spinning head was mounted on an
535 inverted Eclipse Ti2 microscope equipped with a motorized XY Stage (Nikon, Japan).
536 Images were acquired through a 40X NA 1.3 oil objective with a sCMOS camera
537 (Prime95B, Photometrics, USA). Optical sectioning was achieved using a piezo stage
538 (Nano-z series, Mad City Lab, USA). Gataca Systems' laser bench was equipped with
539 405, 491 and 561 nm laser diodes, delivering 150 mW each, coupled to the spinning
540 disk head through a single mode fibre. Multi-dimensional acquisitions were performed
541 using Metamorph 7.10.1 software (Molecular Devices, USA). Stacks of conventional
542 fluorescence images were collected automatically at a Z-distance of 1.5 μ m
543 (Metamorph software; Molecular Devices, RRID:SCR_002368). Images are presented
544 as maximum intensity projections generated with ImageJ software
545 (RRID:SCR_002285).

546

547 *Primary and secondary antibodies*

548 Primary and secondary antibodies were used at the following concentrations: Guinea
549 pig anti CEP192 antibody (1/500; Basto lab)⁵³, rabbit anti beta catenin (1/250; C2206
550 from Sigma-Aldrich, RRID:AB_476831), mouse anti-gamma H2A.X phospho S139
551 (1/1000; ab22551 from Abcam, RRID:AB_447150), mouse anti-XRCC1 (1/500;
552 ab1838 from Abcam, RRID:AB_302636), rabbit anti-Rad51 (1/500; ab133534 from
553 Abcam, RRID:AB_2722613), mouse anti-KU80 (1/200; MA5-12933 from
554 ThermoFisher, RRID:AB_10983840), rabbit anti-FANCD2 (1/150; NB100-182SS from
555 Novusbio, RRID:AB_1108397), rabbit anti- γ H2Av (1/500; 600-401-914 from Rockland;
556 RRID: AB_11183655), Alexa Fluor® 647 Phalloidin (1/250; A22287 from
557 ThermoFisher Scientific, RRID:AB_2620155), goat anti-Rabbit IgG (H+L) Highly
558 Cross-Adsorbed Secondary Antibody, Alexa Fluor 647 (1/250; A21245 from
559 ThermoFisher, RRID:AB_2535813), Goat anti-Guinea Pig IgG (H+L) Highly Cross-
560 Adsorbed Secondary Antibody, Alexa Fluor 488 (1/250; A11073 from ThermoFisher,
561 RRID:AB_253411), Goat anti-Mouse IgG (H+L) Cross-Adsorbed Secondary Antibody,

562 Alexa Fluor 546 (1/250, A11003 from ThermoFisher, RRID:AB_2534071), Goat anti-
563 Rabbit IgG (H+L) Highly Cross-Adsorbed Secondary Antibody, Alexa Fluor 546 (1/250;
564 A-11035 from Thermo Fisher Scientific, RRID:AB_2534093).

565

566 **Quantitative analysis of DNA damage:**

567 *Analysis of Drosophila NBs*

568 Staged 3rd instar larval brains were dissected, stained and imaged using the
569 procedures described above. We used the γ H2Av primary antibody, which was
570 preferentially detected using a secondary antibody conjugated Alexa Fluor 546. We
571 used this secondary antibody because it was found to provide the best signal to noise
572 ratio.

573 Quantitative analysis of DNA damage was carried out as previously described³⁹. In
574 brief, DNA damage was assessed using a γ H2Av primary antibody detected with an
575 Alexa Fluor secondary antibody. Confocal volumes were obtained with optical sections
576 at 1.5 μ m intervals. Image analysis was performed using Fiji and a custom plugin
577 developed by QUANTACELL. After manual segmentation of the nuclei, a thresholding
578 operation was used to determine the percentage of γ H2Av positive pixels (coverage)
579 and their average intensity in a single z plane in the center of the nucleus. Coverage
580 and intensity were multiplied to obtain the γ H2Av index.

581

582 *Analysis of human cell lines*

583 For DNA damage quantification, the signals obtained in cultured cells were different
584 from the signals found in *Drosophila* NBs. To assess DNA damage in human cells, we
585 used an ImageJ software-based plugin developed by QUANTACELL, where γ H2AX
586 signals were measured using z-projection stacks after thresholding. Both FI and the
587 percentage of nuclear coverage was obtained for each nucleus. γ H2AX index was
588 obtained multiplying FI by the coverage.

589

590 All data plotting and statistical analyses were performed using the GraphPad Prism
591 software.

592

593 **Time lapse microscopy:**

594 Cells were plated on a dish (627870 from Dutscher) and treated with the indicated
595 drug. Images were acquired on a spinning disk microscope (Gataca Systems, France).
596 Based on a CSU-W1 (Yokogawa, Japan), the spinning head was mounted on an
597 inverted Eclipse Ti2 microscope equipped with a motorized XY Stage (Nikon, Japan).
598 Images were acquired through a 40X NA 1.3 oil objective with a sCMOS camera
599 (Prime95B, Photometrics, USA). Optical sectioning was achieved using a piezo stage
600 (Nano-z series, Mad City Lab, USA). Gataca Systems' laser bench was equipped with
601 405, 491 and 561 nm laser diodes, delivering 150 mW each, coupled to the spinning
602 disk head through a single mode fiber. Multi-dimensional acquisitions were performed
603 using Metamorph 7.10.1 software (Molecular Devices, USA). Stacks of conventional
604 fluorescence images were collected automatically at a Z-distance of 0.5 μm
605 (Metamorph software; Molecular Devices, RRID:SCR_002368). Images are presented
606 as maximum intensity projections generated with ImageJ software
607 (RRID:SCR_002285), from stacks deconvolved with an extension of Metamorph
608 software.

609

610 **EdU staining:**

611 EdU incorporation into DNA was visualized with the Click-it EdU imaging kit (C10338
612 from Life Technologies), according to the manufacturer's instructions. EdU was used
613 at a concentration of 1 μM (Extended data Fig. 4N and 6E) or 10 μM (Extended data
614 Fig. 4A and I) for the indicated time. Cells were incubated with the Click-it reaction
615 cocktail for 15 minutes.

616

617 **FACS sorting of diploid and tetraploid cells:**

618 A mix of diploid and tetraploid cells (*see "generation of tetraploid cells" section*) were
619 incubated with 2 $\mu\text{g/ml}$ Hoescht (94403 from Sigma Aldrich) for 1 hour at 37°C, 5%
620 CO₂. Then, a single cell suspension was generated. Cells were washed using PBS 1X,
621 the supernatant was removed and cells were resuspended in cold cell culture medium
622 at 1×10^7 cell per ml and kept at 4°C during all the experiment. FACS sorting was
623 performed using Sony SH800 FACS (BD FACSDiva Software Version 8.0.1).
624 Compensation was performed using the appropriate negative control samples.
625 Experimental samples were then recorded and sorted using gating tools to select the
626 populations of interest. RFP+ / GFP- negative cells (G1 cells) were first selected. Then,
627 in this population, DNA content was used to segregate diploid (2n) and tetraploid (4n)

628 G1 cells. Once gates have been determined, diploid and tetraploid G1 cells were
629 sorted into external collection tubes. Post-sort analysis was performed to determine
630 the purity of the sorted populations (see *Extended data Fig. 6A*).

631

632 **E2F1 overexpression:**

633 RPE-1 cells were transfected using 0.25 μ g pCMVHA E2F1 (24225 from Addgene,
634 RRID:Addgene_24225) using JET PRIME kit (Polyplus Transfection, 114-07)
635 according to the manufacturer's protocol. Five hours later, cells were incubated with
636 DMSO (D8418 from Sigma Aldrich) or with 50 μ M monastrol (S8439 from Selleckchem)
637 + 1 μ M MPI-0479605 (S7488 from Selleckchem) to generate tetraploid cells. After 2
638 hours, DMSO or 1 μ M palbociclib (S1579 from Sellechem) were added to the cell
639 culture medium for 16 hours. Cells were then fixed in G1 (T0) or washed five times
640 using PBS and released in S-phase and fixed after 10 hours (T10). The
641 immunofluorescence protocol is described in the corresponding section.

642 pCMVHA E2F1 was a gift from Kristian Helin (Addgene plasmid # 24225 ;
643 <http://n2t.net/addgene:24225> ; RRID:Addgene_24225)⁵⁴.

644

645 **Western Blot analysis and antibodies:**

646 Cells were lysed in 8 M urea, 50 mM Tris HCl, pH 7.5 and 150 mM β -mercaptoethanol
647 (161-0710 from Bio-Rad), sonicated and heated at 95°C for 10 minutes. Samples
648 (equivalent of 2 x 10⁵ cells) were subjected to electrophoresis in NuPAGE Novex 4–
649 12% Bis-Tris pre-cast gels (NP0321 from Life Technologies). Protein fractions from the
650 gel were electrophoretically transferred to PVDF membranes (PVDF transfer
651 membrane; RPN303F from GE). After 1 hr saturation in PBS containing 5% dry non-
652 fat milk and 0.5% Tween 20, the membranes were incubated for 1 hr with a primary
653 antibody (see *below*) diluted in PBS containing 5% dry non-fat milk and 0.5% Tween
654 20. After three 10-min washes with PBS containing 0.5% Tween 20, the membranes
655 were incubated for 45 min with a 1/2 500 dilution of peroxidase-conjugated antibody
656 (see *below*). Membranes were then washed three times with PBS containing 0.5%
657 Tween 20, and the reaction was developed according to the manufacturer's
658 specifications using ECL reagent (SuperSignal West Pico Chemiluminescent
659 Substrate; 34080 from Thermo Scientific). Protein levels were normalized using H2B
660 signal and quantifications were done using Image Lab software version 6.0.1, Bio-Rad
661 Laboratories.

662

663 *Primary and secondary antibodies were used at the following concentrations:*

664 Mouse anti Tubulin (1/5000; T9026 from Sigma, RRID:AB_477593), mouse anti
665 CDC45 (1/500; sc-55569 from Santa Cruz Biotechnology, RRID:AB_831146), rabbit
666 anti PCNA (1/500; sc56 from Santa Cruz, RRID:AB_628110), rabbit anti Actin (1/2000;
667 A5060 from Sigma-Aldrich, RRID:AB_476738), mouse anti-H2B (1/1000; sc-515808
668 from Santa Cruz Biotechnology), mouse anti ORC1 (1/500; sc-398734 from Santa
669 Cruz Biotechnology), mouse anti MCM2 (1/500; 610701 from BD Biosciences,
670 RRID:AB_398024), Goat anti-Rabbit IgG (H+L) Cross-Adsorbed Secondary Antibody,
671 HRP (1/2500; G21234 from ThermoFisher, RRID:AB_2536530), Peroxidase AffiniPure
672 Goat Anti-Mouse IgG (H+L) (1/2500; 115-035-003 from Jackson ImmunoResearch,
673 RRID:AB_10015289).

674

675 **3D reconstruction and analysis on Imaris:**

676 3D movies (see *time lapse microscopy* section) were imported into Imaris software
677 v.9.6.0 (Bitplane, RRID:SCR_007370). For chosen cells, the module “Spot tracking” of
678 Imaris was used to detect the foci, as spots of diameter 0.5 μm in the XY-direction and
679 1 μm in Z-direction (modelling PSF elongation). Because the volume of the foci
680 changes in time, the option “Enable growing regions” was used. In each movie, the
681 threshold was chosen on the brightest frame (to detect a maximum of the correct spots)
682 and then applied to the whole movie. For each cell, at each time point, the number of
683 spots and volumes were recorded. For each condition, at least 10 cells were studied
684 and the statistics from Imaris were averaged at each time point using a MATLAB script.

685

686 **Molecular combing and antibodies:**

687 Tetraploid HCT116 were generated by cytokinesis inhibition using 0.75 μM
688 dihydrocytochalasin D (DCD, inhibitor of actin polymerization, D1641 from Sigma-
689 Aldrich) for 18 h overnight. Afterwards, the cells were washed three times with PBS
690 and cultured in DMEM supplemented with 10% FBS and 1% Pen/Strep for additional
691 10 h. Cells were pulse-labelled with 0.1 mM CldU and 0.1 mM IdU for 30min and 100
692 000 cells per condition were collected for further analysis. The DNA was extracted from
693 cells and prepped following the manufacturer’s instructions using the FiberPrep® DNA
694 Extraction Kit (Genomic Vision, Bagnex, France). Subsequently, the prepped DNA
695 was stretched onto coated glass coverslips (CombiCoverslips™, Genomic Vision,

696 Bagneux, France) by using the FiberComb Molecular Combing System (Genomic
697 Vision, Bagneux, France). The Labelling was performed with antibodies against
698 ssDNA, IdU and CldU using the Replication Combing Assay (RCA) (Genomic Vision,
699 Bagneux, France). The imaging of the prepared cover slips was carried out by
700 Genomic Vision (Bagneux, France) and analysed using the FiberStudio® 2.0.1
701 Analysis Software by Genomic Vision.

702

703 *Antibodies were used at the following concentrations:*

704 Rabbit anti ssDNA (1/5; 18731 from IBL International, RRID:AB_494649), Rat anti
705 CldU (1/10; Ab6326 from Abcam, RRID:AB_2313786), Mouse anti IdU (1/10; 555627
706 from BD Biosciences, RRID:AB_10015222), mouse Alexa Fluor 647 Donkey (1/25;
707 JIM-715-605-151 from Biozol), Rat Alexa Fluor 594 Donkey (1/25; JIM-712-585-153
708 from Biozol), Rabbit Brilliant Violet 480 Donkey (1/25; 711-685-152 from Jackson
709 Immuno Research, RRID:AB_2651109).

710

711 **Quantitative phase imaging and measurements**

712 Cells were plated on glass-bottom dishes coated with 50 µg/ml Fibronectin for 1 hour
713 and rinsed, and trypsinised cells were plated at a concentration of 1.5×10^6 cells/ml. The
714 cells used for the experiments were seeded in T-25 dishes at a concentration of 0.7×10^6
715 cells/ml 2 days before the actual experiment. On the day of the experiment, the cells
716 were detached with EDTA (versene), and plated at a concentration of 1.5×10^6 cells/ml.
717 For inducing tetraploidy, cells were treated with 2µg/ml doxycycline (D3447 from Sigma
718 Aldrich) for 2 hours. Then, 500 µM auxin (I5148 from Sigma Aldrich) + 3µM asunaprevir
719 (S4935 from Selleckchem) was added to the cell culture medium for at least 4 hours.
720 The cells were then imaged for 35 hours every 20 minutes to track them throughout
721 their cell cycle.

722 The cell cycle state of the cells was indicated by the FUCCI system; G1 cells express
723 Cdt1-RFP while S/G2 cells express hGeminin-GFP and mitosis is indicated by the
724 NEBD with geminin being present through the cells⁵⁵. To quantify the fluorescence of
725 geminin in the nucleus, first a background subtraction was performed on the images.
726 An ROI was used to define an area containing the background fluorescence in the
727 image. An average value of the ROI was then subtracted from all the frames.
728 Subsequently, a ROI was drawn as close as possible to the cell, and then the mean

729 gray value was measured across all the frames. This helped identify the frames of birth
730 and G1/S transition during cell cycle.

731 A detailed protocol for the mass measurement with phasics camera is available in ^{56,57}.
732 Images were acquired by Phasics camera every 20 min for 35 hours for the duration
733 of the experiment. To obtain the reference image, 32 empty fields were acquired on
734 the dish and a median image was calculated. This reference image was subtracted
735 from the interferograms (images acquired by phasics) by custom written MATLAB
736 scripts to measure the optical path difference. They were then processed to calculate
737 the phase, intensity and phase cleaned images (the background set to 1000 and the
738 field cropped to remove edges). Background normalization was performed using a
739 gridfit method and a watershed algorithm was used to separate cells which came in
740 contact with each other. Mass was calculated by integrating the intensity of the whole
741 cell.

742

743 **Sequencing and AneuFinder analysis:**

744 A mixed population of diploid and tetraploid RPE-1 CCNB1^{AID} FUCCI cells were
745 synchronized in G1 using 1 μ M palbociclib (S1579 from Selleckchem) for 16 hours or
746 released in S-phase for 20 hours in the presence of 10 μ M RO3306 (217699 from
747 Calbiochem) in order to block cells in the subsequent G2/M. G1 and G2/M diploid and
748 tetraploid cells were then isolated using cell sorting (see “*FACS sorting of diploid and*
749 *tetraploid cells*” section) and collected in a 96-well plate. Single-cell sequencing was
750 performed as described in detail in ⁵⁸. Briefly, cells were lysed to prepare a suspension
751 of nuclei and sorted as single nuclei in 96 or 384 well plates. Next, single cell
752 sequencing libraries were prepared using a semi-automated liquid handler platform
753 (Bravo, Agilent technologies). For library preparation, chromatin was fragmented by
754 micrococcal nuclease, end-repaired, and A-tailed, followed by Illumina adapter ligation.
755 Libraries were then cleaned up and PCR-amplified for 17 cycles that included the
756 addition of a library-specific barcode to uniquely label individual cell libraries. Up to 384
757 libraries were pooled and sequenced on a Nextseq 500 machine (Illumina; up to 77
758 cycles; single end). The generated data were subsequently demultiplexed using
759 sample-specific barcodes and changed into fastq files using bcl2fastq (Illumina;
760 version 1.8.4). Reads were afterwards aligned to the human reference genome
761 (GRCh38/hg38) using Bowtie2 (version 2.2.4)⁵⁹. Duplicate reads were marked with
762 BamUtil (version 1.0.3)⁶⁰. The aligned read data (bam files) were analyzed with a copy

763 number calling algorithm called AneuFinder (<https://github.com/ataudt/aneufinder>)⁶¹.
764 Following GC correction and blacklisting of artefact-prone regions (extreme low or high
765 coverage in control samples), libraries were analyzed using the dnacopy and edivisive
766 copy number calling algorithms with variable width bins (average binsize = 1 Mb; step
767 size = 500 kb). The G1 samples were used as reference for the analysis of the G2/M
768 samples (G1 diploid for G2/M diploid and G1 polyploid for G2/M polyploid). The G1
769 samples were analyzed with an euploid reference⁶². Results were afterwards curated
770 by requiring a minimum concordance of 90 % (4N and 8N samples) or 95% (2N
771 samples) between the results of the two algorithms. Libraries with on average less than
772 10 reads per bin (~ 30,000 reads for a diploid genome) were discarded. The aneuploidy
773 scores corresponds to the absolute difference from euploid genome and is the average
774 from all bins and all libraries of one sample. Heterogeneity scores is calculated as the
775 proportion of pairwise comparisons, between libraries, that shows different copy
776 numbers. This is first calculated for each bin. To get to the final score a weighted
777 average is applied.

778

779 **QUANTIFICATION AND STATISTICAL ANALYSIS:**

780

781 *Quantifications:*

782 Image analysis and quantifications were performed using Image J software
783 V2.1.0/1.53c, <https://imagej.net/software/fiji/downloads>. To quantify the colocalizations
784 between two signals (Extended data Fig. 3M and 4D) we used *JACOP* plugin with
785 Image J software. 3D movies (Fig. 2F and Extended data Fig. 3B) were corrected using
786 *3D correct drift* plugin with Image J software to keep the cell of interest at the centre of
787 the region of interest. The nuclear area and DAPI intensity were measured using the
788 *wand* tool with Image J software. For the figures, images were processed on Image J
789 software, and mounted using Affinity Designer, <https://affinity.serif.com/fr/designer/>.

790

791 *Statistical analysis:*

792 At least three (n) independent experiments were carried out to generate each dataset,
793 and the statistical significance of differences was calculated with Student's t-test.
794 These tests were performed using GraphPad Prism (RRID:SCR_002798) version 7.00
795 for Mac, GraphPad Software, La Jolla California USA, www.graphpad.com.

796

798 **REFERENCES:**

799

- 800 1. Zack, T. I. *et al.* Pan-cancer patterns of somatic copy number alteration. *Nat.*
801 *Genet.* **45**, 1134–1140 (2013).
- 802 2. Bielski, C. M. *et al.* Genome doubling shapes the evolution and prognosis of
803 advanced cancers. *Nat. Genet.* **50**, 1189–1195 (2018).
- 804 3. López, S. *et al.* Interplay between whole-genome doubling and the
805 accumulation of deleterious alterations in cancer evolution. *Nat. Genet.* **52**,
806 283–293 (2020).
- 807 4. Storchova, Z. & Kuffer, C. The consequences of tetraploidy and aneuploidy.
808 *Journal of Cell Science* vol. 121 3859–3866 (2008).
- 809 5. Storchova, Z. & Pellman, D. From polyploidy to aneuploidy, genome instability
810 and cancer. *Nature Reviews Molecular Cell Biology* vol. 5 45–54 (2004).
- 811 6. Dewhurst, S. M. *et al.* Tolerance of whole- genome doubling propagates
812 chromosomal instability and accelerates cancer genome evolution. *Cancer*
813 *Discov.* **4**, 175–185 (2014).
- 814 7. Fox, D. T., Gall, J. G. & Spradling, A. C. Error-prone polyploid mitosis during
815 normal *Drosophila* development. *Genes Dev.* **24**, 2294–2302 (2010).
- 816 8. Goupil, A. *et al.* Chromosomes function as a barrier to mitotic spindle bipolarity
817 in polyploid cells. *J. Cell Biol.* **219**, (2020).
- 818 9. Crockford, A. *et al.* Cyclin D mediates tolerance of genome-doubling in cancers
819 with functional p53. *Ann. Oncol.* **28**, 149–156 (2017).
- 820 10. Potapova, T. A., Seidel, C. W., Box, A. C., Rancati, G. & Li, R. Transcriptome
821 analysis of tetraploid cells identifies cyclin D2 as a facilitator of adaptation to
822 genome doubling in the presence of p53. *Mol. Biol. Cell* **27**, 3065–3084 (2016).
- 823 11. Andreassen, P. R., Lohez, O. D., Lacroix, F. B. & Margolis, R. L. Tetraploid
824 state induces p53-dependent arrest of nontransformed mammalian cells in G1.
825 *Mol. Biol. Cell* **12**, 1315–1328 (2001).
- 826 12. Storchová, Z. *et al.* Genome-wide genetic analysis of polyploidy in yeast.
827 *Nature* **443**, 541–547 (2006).
- 828 13. Carter, S. L. *et al.* Absolute quantification of somatic DNA alterations in human
829 cancer. *Nat. Biotechnol.* **30**, 413–421 (2012).
- 830 14. Ganem, N. J., Storchova, Z. & Pellman, D. Tetraploidy, aneuploidy and cancer.
831 *Current Opinion in Genetics and Development* vol. 17 157–162 (2007).

- 832 15. Gemble, S. & Basto, R. CHRONOCRISIS: When Cell Cycle Asynchrony
833 Generates DNA Damage in Polyploid Cells. *BioEssays* **42**, (2020).
- 834 16. Kuznetsova, A. Y. *et al.* Chromosomal instability, tolerance of mitotic errors and
835 multidrug resistance are promoted by tetraploidization in human cells. *Cell*
836 *Cycle* **14**, 2810–2820 (2015).
- 837 17. Jemaà, M. *et al.* Whole-genome duplication increases tumor cell sensitivity to
838 MPS1 inhibition. *Oncotarget* **7**, 885–901 (2016).
- 839 18. Quinton, R. J. *et al.* Whole-genome doubling confers unique genetic
840 vulnerabilities on tumour cells. *Nature* **590**, 492–497 (2021).
- 841 19. Fujiwara, T. *et al.* Cytokinesis failure generating tetraploids promotes
842 tumorigenesis in p53-null cells. *Nature* **437**, 1043–1047 (2005).
- 843 20. Orr-Weaver, T. L. When bigger is better: The role of polyploidy in
844 organogenesis. *Trends in Genetics* vol. 31 307–315 (2015).
- 845 21. Zeman, M. K. & Cimprich, K. A. Causes and Consequences of Replication
846 Stress. *Nat. Cell Biol.* **16**, 2 (2014).
- 847 22. Koundrioukoff, S. *et al.* Stepwise activation of the ATR signaling pathway upon
848 increasing replication stress impacts fragile site integrity. *PLoS Genet.* **9**,
849 e1003643 (2013).
- 850 23. Panier, S. & Boulton, S. J. Double-strand break repair: 53BP1 comes into
851 focus. *Nat. Rev. Mol. Cell Biol.* **15**, 7–18 (2014).
- 852 24. Zhao, B., Rothenberg, E., Ramsden, D. A. & Lieber, M. R. The molecular basis
853 and disease relevance of non-homologous DNA end joining. *Nat. Rev. Mol.*
854 *Cell Biol.* **21**, 765–781 (2020).
- 855 25. A, B., T, L. & A, C. Quantitative live imaging of endogenous DNA replication in
856 mammalian cells. *PLoS One* **7**, (2012).
- 857 26. Michalet, X. *et al.* Dynamic molecular combing: Stretching the whole human
858 genome for high- resolution studies. *Science (80-.).* **277**, 1518–1523 (1997).
- 859 27. Zlotek-Zlotkiewicz, E., Monnier, S., Cappello, G., Berre, M. Le & Piel, M.
860 Optical volume and mass measurements show that mammalian cells swell
861 during mitosis. *J. Cell Biol.* **211**, 765 (2015).
- 862 28. Tatsumi, Y., Ohta, S., Kimura, H., Tsurimoto, T. & Obuse, C. The ORC1 cycle
863 in human cells: I. Cell cycle-regulated oscillation of human ORC1. *J. Biol.*
864 *Chem.* **278**, 41528–41534 (2003).
- 865 29. Remus, D. *et al.* Concerted Loading of Mcm2-7 Double Hexamers around DNA

- 866 during DNA Replication Origin Licensing. *Cell* **139**, 719–730 (2009).
- 867 30. Moyer, S. E., Lewis, P. W. & Botchan, M. R. Isolation of the Cdc45/Mcm2-
868 7/GINS (CMG) complex, a candidate for the eukaryotic DNA replication fork
869 helicase. *Proc. Natl. Acad. Sci. U. S. A.* **103**, 10236–10241 (2006).
- 870 31. Bertoli, C., Skotheim, J. M. & De Bruin, R. A. M. Control of cell cycle
871 transcription during G1 and S phases. *Nature Reviews Molecular Cell Biology*
872 vol. 14 518–528 (2013).
- 873 32. Pardee, A. B. G1 events and regulation of cell proliferation. *Science (80-.)*.
874 **246**, 603–608 (1989).
- 875 33. Cadart, C. *et al.* Size control in mammalian cells involves modulation of both
876 growth rate and cell cycle duration. *Nat. Commun.* **9**, (2018).
- 877 34. DW, F. *et al.* Specific inhibition of cyclin-dependent kinase 4/6 by PD 0332991
878 and associated antitumor activity in human tumor xenografts. *Mol. Cancer*
879 *Ther.* **3**, 1427–1437 (2004).
- 880 35. Tan, C. *et al.* Cell size homeostasis is maintained by CDK4-dependent
881 activation of p38 MAPK. *Dev. Cell* **56**, 1756-1769.e7 (2021).
- 882 36. Charvin, G., Oikonomou, C., Siggia, E. D. & Cross, F. R. Origin of irreversibility
883 of cell cycle start in budding yeast. *PLoS Biol.* **8**, (2010).
- 884 37. Cross, F. R., Buchler, N. E. & Skotheim, J. M. Evolution of networks and
885 sequences in eukaryotic cell cycle control. *Philosophical Transactions of the*
886 *Royal Society B: Biological Sciences* vol. 366 3532–3544 (2011).
- 887 38. Zatulovskiy, E., Zhang, S., Berenson, D. F., Topacio, B. R. & Skotheim, J. M.
888 Cell growth dilutes the cell cycle inhibitor Rb to trigger cell division. *Science*
889 (80-.). **369**, 466–471 (2020).
- 890 39. Nano, M. *et al.* Cell-Cycle Asynchrony Generates DNA Damage at Mitotic
891 Entry in Polyploid Cells. *Curr. Biol.* **29**, (2019).
- 892 40. Frawley, L. E. & Orr-Weaver, T. L. Polyploidy. *Current Biology* vol. 25 R353–
893 R358 (2015).
- 894 41. Tseng, A.-S. K. & Hariharan, I. K. *An Overexpression Screen in Drosophila for*
895 *Genes That Restrict Growth or Cell-Cycle Progression in the Developing Eye.*
896 (2002).
- 897 42. Duronio, R. J., Brook, A., Dyson, N. & O’Farrell, P. H. E2F-induced S phase
898 requires cyclin E. *Genes Dev.* **10**, 2505–2513 (1996).
- 899 43. Maya-Mendoza, A. *et al.* High speed of fork progression induces DNA

- 900 replication stress and genomic instability. *Nature* **559**, 279–284 (2018).
- 901 44. Sedlackova, H. *et al.* Equilibrium between nascent and parental MCM proteins
902 protects replicating genomes. *Nature* **587**, 297–302 (2020).
- 903 45. M, T. *et al.* Functional reprogramming of polyploidization in megakaryocytes.
904 *Dev. Cell* **32**, 155–167 (2015).
- 905 46. Klusza, S. & Deng, W.-M. At the crossroads of differentiation and proliferation:
906 Precise control of cell-cycle changes by multiple signaling pathways in
907 *Drosophila* follicle cells. *Bioessays* **33**, 124 (2011).
- 908 47. Viganó, C. *et al.* Quantitative proteomic and phosphoproteomic comparison of
909 human colon cancer DLD-1 cells differing in ploidy and chromosome stability.
910 *Mol. Biol. Cell* **29**, 1031–1047 (2018).
- 911 48. Wangsa, D. *et al.* Near-tetraploid cancer cells show chromosome instability
912 triggered by replication stress and exhibit enhanced invasiveness. *FASEB J.*
913 **32**, 3502–3517 (2018).
- 914 49. Hégarat, N. *et al.* Cyclin A triggers Mitosis either via the Greatwall kinase
915 pathway or Cyclin B. *EMBO J.* **39**, (2020).
- 916 50. SB, K. *et al.* A quantitative FastFUCCI assay defines cell cycle dynamics at a
917 single-cell level. *J. Cell Sci.* **130**, 512–520 (2017).
- 918 51. KS, Y., RH, K., M, L., R, G. & R, W. Single cell resolution in vivo imaging of
919 DNA damage following PARP inhibition. *Sci. Rep.* **5**, (2015).
- 920 52. Karess, R. E. *et al.* The regulatory light chain of nonmuscle myosin is encoded
921 by spaghetti-squash, a gene required for cytokinesis in *Drosophila*. *Cell* **65**,
922 1177–1189 (1991).
- 923 53. Gemble, S. *et al.* Centromere Dysfunction Compromises Mitotic Spindle Pole
924 Integrity. *Curr. Biol.* **29**, (2019).
- 925 54. J, L., BO, P., K, H., J, B. & K, H. Deregulated expression of E2F family
926 members induces S-phase entry and overcomes p16INK4A-mediated growth
927 suppression. *Mol. Cell. Biol.* **16**, 1047–1057 (1996).
- 928 55. Sakaue-Sawano, A. *et al.* Visualizing Spatiotemporal Dynamics of Multicellular
929 Cell-Cycle Progression. *Cell* **132**, 487–498 (2008).
- 930 56. Aknoun, S. *et al.* Living cell dry mass measurement using quantitative phase
931 imaging with quadriwave lateral shearing interferometry: an accuracy and
932 sensitivity discussion. *J. Biomed. Opt.* **20**, 126009 (2015).
- 933 57. Bon, P., Maucort, G., Wattellier, B. & Monneret, S. Quadriwave lateral shearing

- 934 interferometry for quantitative phase microscopy of living cells. *Opt. Express*
935 **17**, 13080 (2009).
- 936 58. van den Bos, H. *et al.* Quantification of aneuploidy in mammalian systems. in
937 *Methods in Molecular Biology* vol. 1896 159–190 (Humana Press Inc., 2019).
- 938 59. Langmead, B. & Salzberg, S. L. Fast gapped-read alignment with Bowtie 2.
939 *Nat. Methods* **9**, 357–359 (2012).
- 940 60. Jun, G., Wing, M. K., Abecasis, G. R. & Kang, H. M. An efficient and scalable
941 analysis framework for variant extraction and refinement from population-scale
942 DNA sequence data. *Genome Res.* **25**, 918–925 (2015).
- 943 61. Bakker, B. *et al.* Single-cell sequencing reveals karyotype heterogeneity in
944 murine and human malignancies. *Genome Biol.* **17**, (2016).
- 945 62. van den Bos, H. *et al.* Single-cell whole genome sequencing reveals no
946 evidence for common aneuploidy in normal and Alzheimer’s disease neurons.
947 *Genome Biol.* **17**, 1–9 (2016).
- 948

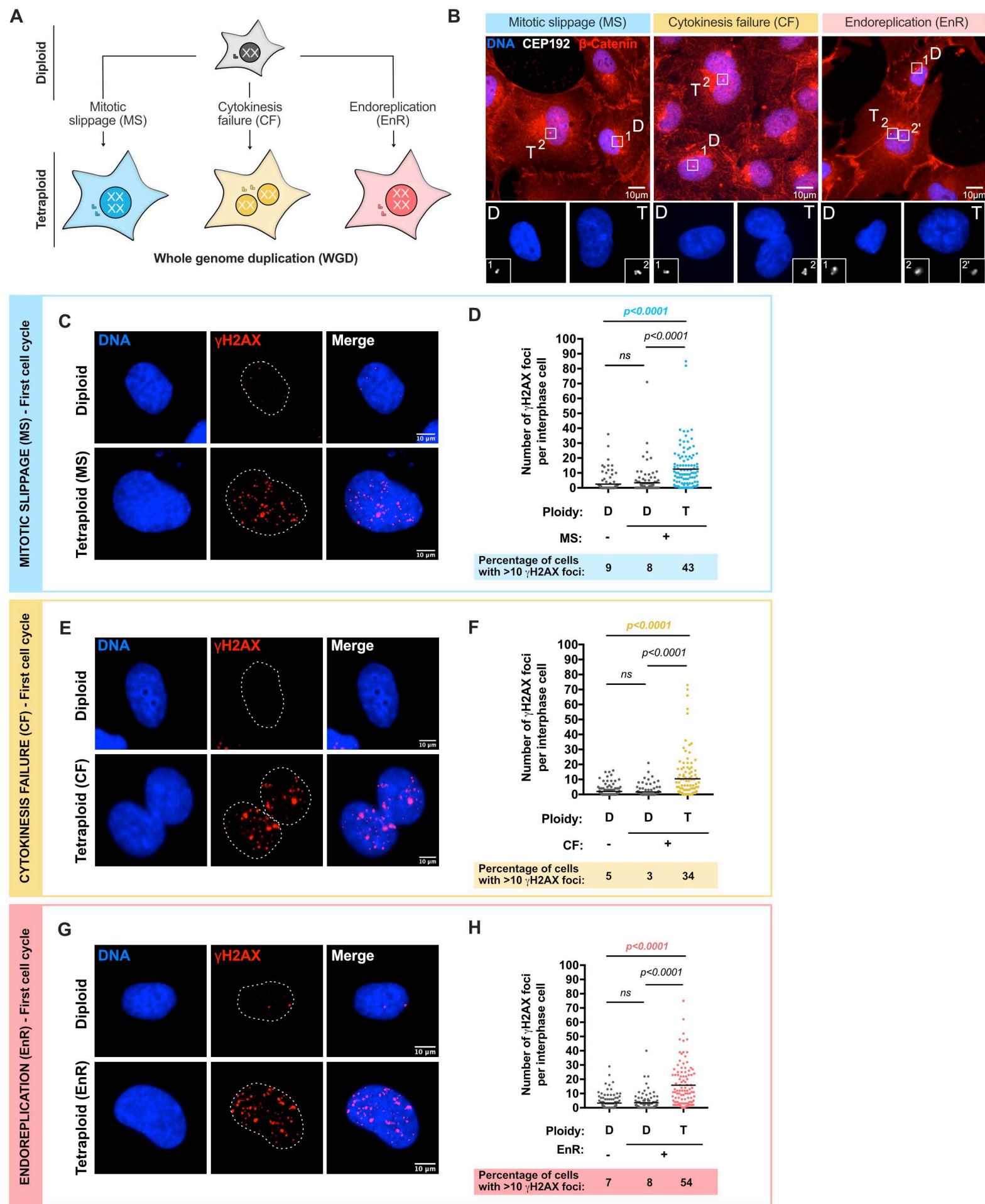


Figure 1: High levels of DNA damage are generated in the first interphase following unscheduled WGD.

(A) Schematic representation of the generation of tetraploid cells. **(B)** Representative immunofluorescence images of diploid and tetraploid RPE-1 cells generated by inhibiting Eg5 and MPS1 (MS), or MKLP1 (CF), or JNK (EnR). DNA was visualized using DAPI (in blue), centrosomes were stained using anti-CEP192 antibodies (in white) and membranes were stained using anti- β -Catenin antibodies (in red). The white squares correspond to higher magnifications presented in the lower panel and showing the centrosomes (in yellow). **(C, E and G)** Representative immunofluorescence images showing DNA damage in diploid and tetraploid RPE-1 cells were generated by inhibiting Eg5 and MPS1 (MS), or MPS1 (CF), or JNK (EnR). DNA was visualized using DAPI (in blue), DNA damage was visualized using anti- γ H2AX antibodies (in red). >100 interphase cells were analyzed from at least three independent experiments. **(D, F and H)** Graph showing the number of γ H2AX foci per interphase cells in diploid and tetraploid RPE-1 cells. The percentage of interphase cells with more than 10 γ H2AX foci in diploid and tetraploid RPE-1 cells were indicated under the graph. >100 interphase cells were analyzed from at least three independent experiments. The dotted lines indicate the nuclear area. D: Diploid. T: Tetraploid. MS: mitotic slippage. CF: cytokinesis failure. EnR: endoreplication.

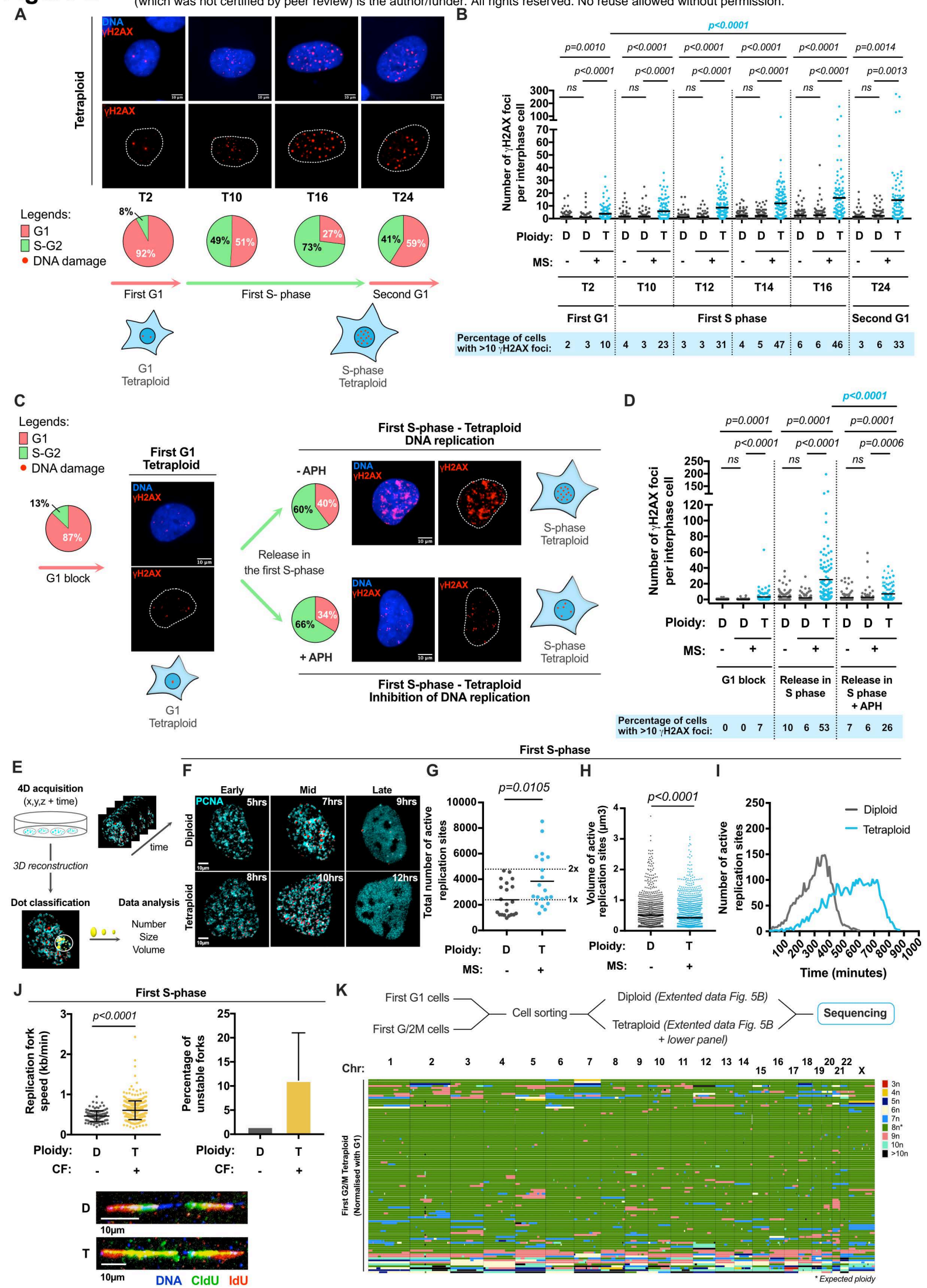


Figure 2: DNA damage and genetic instability in tetraploid cells is generated during S-phase in a DNA replication-dependent manner.

(A) Upper panel - Representative immunofluorescence images showing DNA damage in RPE-1 tetraploid cells over time. DNA was visualized using DAPI (in blue), DNA damage is visualized using anti- γ H2AX antibodies (in red). Lower panel - Percentage of RPE-1 FUCCI tetraploid cells in G1 (red) or in S-G2 (green) over time. **(B)** Graph representing the number of γ H2AX foci per interphase cells in diploid (gray) and tetraploid (blue) RPE-1 cells over time. The percentage of interphase cells with more than 10 γ H2AX foci in diploid and tetraploid RPE-1 cells is indicated under the graph. >100 interphase cells were analyzed from at least three independent experiments. **(C)** Percentage of RPE-1 FUCCI tetraploid cells in G1 (red) or in S-G2 (green) and representative immunofluorescence images showing DNA damage in tetraploid cells synchronized in G1 using 1 μ M palbociclib or released in S-phase with or without 400nM aphidicolin (APH). DNA was visualized using DAPI (in blue), DNA damage was visualized using anti- γ H2AX antibodies (in red). **(D)** Graph showing the number of γ H2AX foci per interphase cells in diploid (gray) and tetraploid (blue) RPE-1 cells synchronized in G1 using 1 μ M palbociclib or released in S-phase with or without 400nM aphidicolin (APH). The percentage of interphase cells with more than 10 γ H2AX foci in diploid and tetraploid RPE-1 cells are indicated under the graph. >100 interphase cells were analyzed from at least three independent experiments. **(E)** Schematic workflow showing the method used in this study to process and analyze DNA replication by live imaging. **(F)** Stills of time lapse of diploid and tetraploid RPE-1 PCNA^{chromo} cells. Active replication sites are visualized using PCNA chromobodies (in cyan) and reconstructed using Imaris in 3D (in red). **(G)** Graph showing the total number of active replication sites during S-phase in diploid (gray) and tetraploid (blue) RPE-1 cells. >20 S-phase cells were analyzed from three independent experiments. **(H)** Graph showing the volume of active replication sites in μm^3 in diploid (gray) and tetraploid (blue) RPE-1 PCNA^{chromo} cells. At least 1000 active replication sites were analyzed. **(I)** Graph showing the mean number of active replication sites over time in diploid (gray line) and tetraploid (blue line) RPE-1 cells. >20 S-phase cells were analyzed from three independent experiments. For other representative examples, see Figure S5A. **(J)** Left panel - Graph representing the replication fork speed in diploid (gray) and tetraploid (yellow) HCT116 cells. Right panel - Graph showing the percentage of unstable replication forks in diploid (gray) and tetraploid (yellow) HCT116 cells. More than 120 replication forks were analyzed. Lower panel - Representative immunofluorescence of DNA fibers obtained from diploid and tetraploid HCT116 cells. ssDNA was visualized using anti-ssDNA antibodies (in blue), CldU and IdU was visualized using anti-IdU and anti-CldU antibodies (in red and green), respectively. **(K)** Genome-wide copy number plots G2/M tetraploid RPE-1 cells were generated using a modified version of the Aneupfinder algorithm and normalized using G1 tetraploid cells (see methods). Each row represents a cell and the copy number state (in 5-Mb bins) is indicated in colors (with aberrations contrasting from from dark green in G2/M (8n)). The dotted lines indicate nuclear area. D: Diploid. T: Tetraploid. MS: mitotic slippage. CF: cytokinesis failure. EnR: endoreplication.

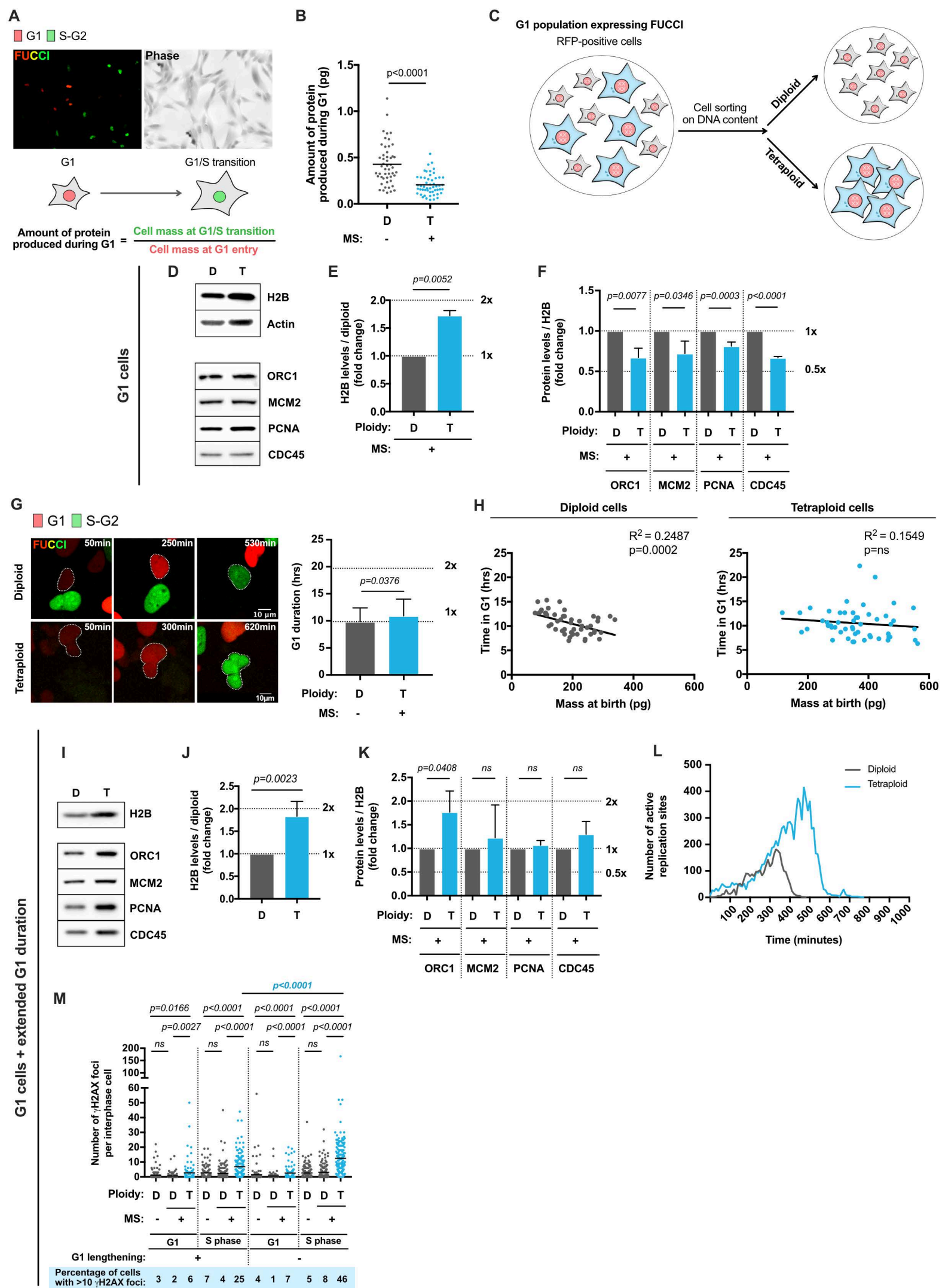


Figure 3: Lack of G1 lengthening in tetraploid cells leads to unprepared S-phase.

(A) Stills of time lapse of RPE CCNB1^{AID} FUCCI diploid and tetraploid cells. G1 cells are in red and S-G2 cells are in green. **(B)** Graph representing the amount of protein produced during G1 in diploid (gray) and tetraploid (blue) RPE-1 CCNB1^{AID} FUCCI cells. **(C)** Schematic representation of cell sorting of G1 diploid and tetraploid cells. At least 50 cells were analyzed. **(D)** H2B, actin, ORC1, MCM2, PCNA and Cdc45 levels assessed by western blot of cell lysates obtained from diploid (left) and tetraploid (right) RPE-1 CCNB1^{AID} FUCCI cells. The same number of cells was loaded for each condition. **(E)** Graph showing H2B levels normalized with diploid condition (fold change) in diploid (gray) and tetraploid (blue) cells. Mean +/- sd representing three independent experiments. **(F)** Graph representing the protein levels relative to H2B levels (fold change) in diploid (gray) and tetraploid (blue) cells. Mean +/- sd representing three independent experiments. **(G)** Left panel – Stills of time lapse of RPE FUCCI diploid and tetraploid cells. G1 cells are in red and S-G2 cells are in green. Right panel - Graph showing the time in G1 compared to the mass at birth in diploid (left panel, gray) and tetraploid (right panel, blue) RPE-1 FUCCI cells. At least 55 interphase cells from two independent experiments were analyzed. **(H)** Graph showing the correlation between the time in G1 and the mass at birth in diploid and tetraploid RPE-1 CCNB1^{AID} FUCCI cells. At least 50 interphase cells were analyzed. **(I)** H2B, ORC1, MCM2, PCNA and Cdc45 levels assessed by western blot of cell lysates obtained from diploid (left) and tetraploid (right) RPE-1 CCNB1^{AID} FUCCI cells with extended G1 duration. The same number of cells was loaded for each condition. **(J)** Graph showing H2B levels normalized with diploid condition (fold change) in diploid (gray) and tetraploid (blue) cells with extended G1 duration. Mean +/- sd representing three independent experiments. **(K)** Graph representing the protein levels relative to H2B levels (fold change) in diploid (gray) and tetraploid (blue) cells with extended G1 duration. Mean +/- sd representing three independent experiments. **(L)** Graph showing the average number of active replication sites over time in diploid (gray line) or tetraploid (blue line) RPE PCNA^{chromo} cells with extended G1 duration. For other representative examples, see Figure S6L. **(M)** Graph showing the number of γ H2AX foci in interphase cells in diploid (gray) and tetraploid cells (blue) synchronized in G1 using 160nM (extended G1 duration) or 1 μ M (G1 arrest) palbociclib or released in S-phase. At least 100 interphase cells were analyzed from three independent experiments. D: Diploid. T: Tetraploid. MS: mitotic slippage.

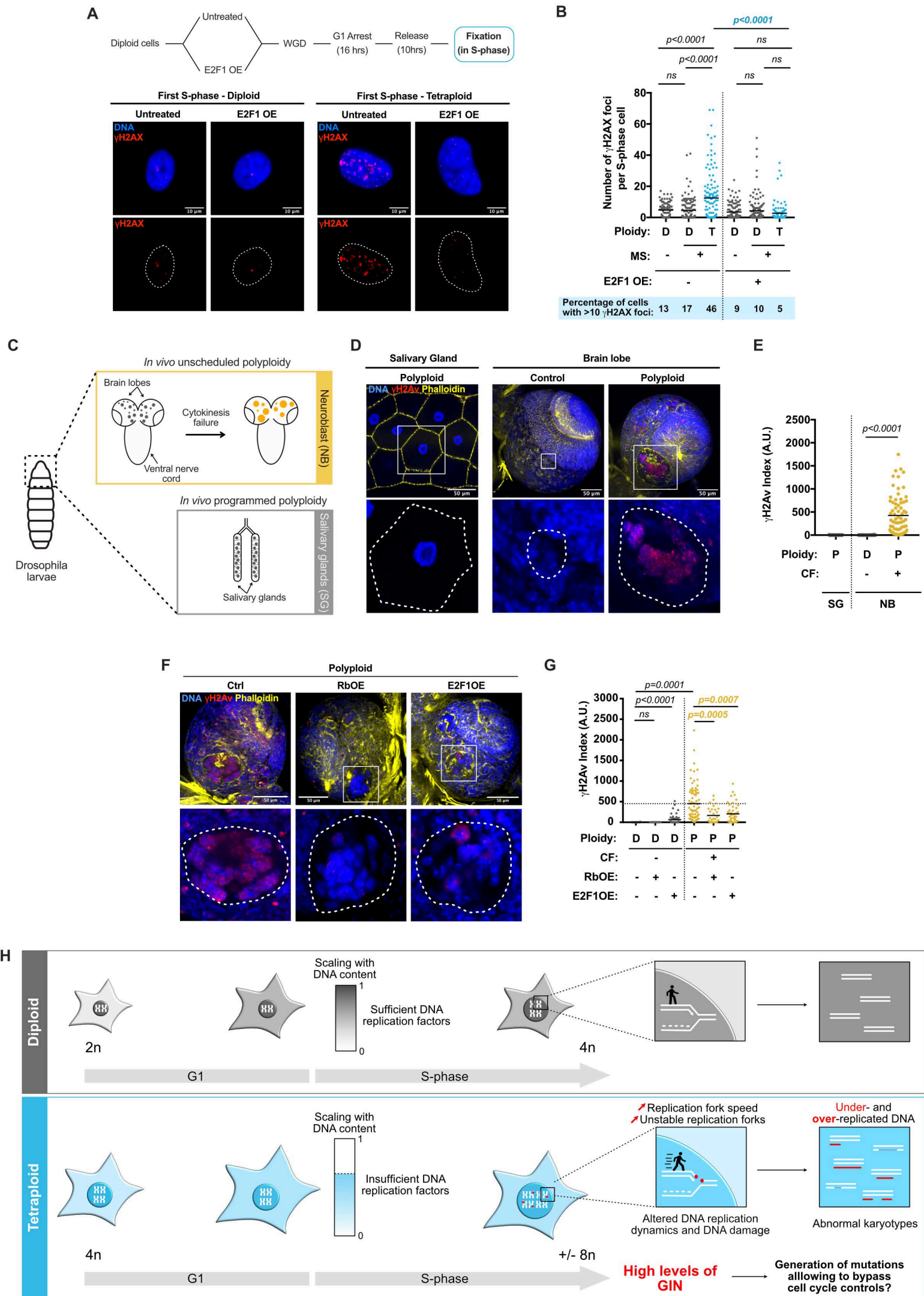


Figure 4: G1 lengthening or increased E2F1 levels are sufficient to rescue GIN in tetraploid cells and in polyploid cells *in vivo*.

(A) Upper panel - Schematic workflow showing the method used to overexpress E2F1. Lower panel - Representative immunofluorescence images showing DNA damage in RPE-1 tetraploid cells overexpressing or not E2F1. DNA was visualized using DAPI (in blue), DNA damage was visualized using anti- γ H2AX antibodies (in red). **(B)** Graph showing the number of γ H2AX foci per interphase cells in diploid (gray) and tetraploid (blue) RPE-1 cells released in S-phase with or without E2F1 overexpression. The percentage of interphase cells with more than 10 γ H2AX foci in diploid and tetraploid RPE-1 cells were indicated under the graph. >100 interphase cells were analyzed from at least three independent experiments. **(C)** Schematic representation of the brain of *drosophila* larvae. **(D)** Representative immunofluorescence images of *drosophila* brain lobe in control or *sqh* mutant (polyploid) and of salivary glands. DNA was visualized using DAPI (in blue), DNA damage was visualized using anti- γ H2Av antibodies (in red), membranes were visualized using Phalloidin (in yellow). **(E)** γ H2Av index in *drosophila* salivary glands (SG, gray) or in diploid (gray) and polyploid (yellow) neuroblasts (NB). At least 60 cells were analyzed per condition. **(F)** Representative immunofluorescence images of *drosophila* brain lobe in control or *sqh* mutant (polyploid) overexpressing or not E2F1. DNA was visualized using DAPI (in blue), DNA damage was visualized using anti- γ H2Av antibodies (in red), membranes were visualized using Phalloidin (in yellow). **(G)** Graph showing the γ H2Av index in diploid (gray) and polyploid (yellow) *drosophila* neuroblasts overexpressing or not E2F1. At least 30 cells were analyzed per condition. **(H)** Tetraploid cells are not able to sense an increase in DNA content and to adapt G1 duration. In consequence, G1 duration is not scaled up with DNA content and tetraploid cells enter S-phase with an insufficient amount of replication factors generating DNA replication-dependent DNA damage and abnormal karyotypes. The dotted lines indicate the nuclear (B) or cell area (D and F). The white squares correspond to higher magnifications presented in the lower panel. D: Diploid. T: Tetraploid. P: Polyploid. CF: cytokinesis failure. MS: mitotic slippage.